Materials Letters 363 (2024) 136277

Contents lists available at ScienceDirect

Materials Letters

journal homepage: www.elsevier.com/locate/matlet

Precipitation behavior of the $M_{23}C_6$ phase on the coherent twin boundary of 25Cr-20Ni-Nb-N steel

Tomotaka Hatakeyama *, Kota Sawada

Research Center for Structural Materials, National Institute for Materials Science, 1-2-1, Sengen, Tsukuba, Ibaraki, 305-0047, Japan

ARTICLE INFO

Keywords:
Austenitic steel
Carbide
Coherent precipitation
Twin boundary

ABSTRACT

The precipitation behavior of $M_{23}C_6$ on random and coherent twin boundaries in aged 25Cr–20Ni–Nb–N steel was characterized. $M_{23}C_6$ on a random boundary has a cube-on-cube orientation relationship with a single-grain side and no orientation relationship with the other side. NbX was precipitated at the coherent interface on the random boundary. Two $M_{23}C_6$ particles were precipitated on both sides of the coherent twin boundary with a $(1\,1\,1)_{M23C6\text{-}A}//(1\,1\,1)_{M23C6\text{-}B}$ and $[1\,1\,0]_{M23C6\text{-}A}//[1\,1\,0]_{M23C6\text{-}B}$ orientation relationship, which is identical with that of the coherent twin boundary of austenite matrix. As a result, the $M_{23}C_6$ twin was formed at the original twin boundary. Both sides of the matrix/$M_{23}C_6$ interfaces satisfied a cube-on-cube orientation relationship with faceted interfaces parallel to $(1\,1\,1)_\gamma$ and $(1\,1\,1)_{M23C6}$. NbX is precipitated at the $M_{23}C_6$ twin boundary.

1. Introduction

The 25Cr–20Ni–Nb–N steel (KA-SUS310J1TB, ASME TP310HCbN) is an austenitic stainless steel extensively used for boiler tubes in ultra-supercritical and waste-to-power plants [1–3]. However, this steel material exhibits poor creep ductility manifested by intergranular creep failure [4]. Therefore, microstructural control is desired to suppress the intergranular creep failure.

$M_{23}C_6$ (M is mainly Cr) is a major precipitate in austenitic steels with a complex face-centered cubic structure. Recently, Hatakeyama et al. [5,6] revealed that $M_{23}C_6$ precipitated on a grain boundary during creep deformation reduced the creep rate of austenitic steels by grain boundary precipitation strengthening. More recently, Hatakeyama et al. [7] clarified that the coherent matrix/$M_{23}C_6$ interface along the (1 1 1) plane with cube-on-cube precipitation of $M_{23}C_6$ on the random boundary (RB) of 25Cr–20Ni–Nb–N steel has extensive crack propagation arrestability. This results in preferential crack propagation along the incoherent matrix/$M_{23}C_6$ interface on the other side. These authors also revealed that a sufficiently high area fraction of $M_{23}C_6$ on a grain boundary (~90 %), fragmented the crack propagation path (uncovered RB and incoherent matrix/$M_{23}C_6$ interface), disturbed the percolation of intergranular cracks, and resulted in enhanced creep strength and ductility. However, the rapid coarsening kinetics of $M_{23}C_6$ on RB is concerning as it may not preserve a sufficiently high area fraction of $M_{23}C_6$ on the grain boundary during long-term creep exposure.

Polycrystalline austenitic steels contain coherent twin boundary (CTB) in addition to RB. CTB has an orientation relationship (OR) of $(1\,1\,1)_{\gamma1}//(1\,1\,1)_{\gamma2}$ and $[1\,1\,0]_{\gamma1}//[1\,1\,0]_{\gamma2}$ and is considered as an Σ3 coincidence site lattice (CSL) boundary [8]. The frequency of CSL boundaries of austenitic steels can increase by grain boundary engineering (GBE) [9]. It is reported that plate-like $M_{23}C_6$ coherently grew on CTB [10]; therefore, both sides of the matrix/$M_{23}C_6$ interfaces are expected to have high-crack propagation arrestability and slower coarsening kinetics. However, to the best of our knowledge, the detailed precipitation behavior of $M_{23}C_6$ on the CTB has not been well understood. This study clarifies the precipitation behavior of $M_{23}C_6$ on the CTB to enhance further the creep properties through the synergy of GBE and coherent matrix/$M_{23}C_6$ interface on CTB.

2. Experimental procedures

The sample material was a 25Cr–20Ni–Nb–N steel tube. Its chemical composition was 0.06C–0.41Si–1.25Mn–0.018P–0.001S –19.84Ni–24.60Cr–0.46Nb–0.272 N (mass%) [4]. Processing details are described in [4]. As-received steel was aged at 973 K for 500 h and cooled in a furnace. The microstructure of the aged steel was characterized by scanning electron microscopy (SEM), SEM-electron backscatter diffraction (SEM-EBSD), transmission electron microscopy (TEM), scanning TEM (STEM), and STEM-energy dispersive X-ray spectroscopy (STEM-EDS).

* Corresponding author.
E-mail address: hatakeyama.tomotaka@nims.go.jp (T. Hatakeyama).

https://doi.org/10.1016/j.matlet.2024.136277
Received 15 February 2024; Received in revised form 6 March 2024; Accepted 7 March 2024
Available online 7 March 2024

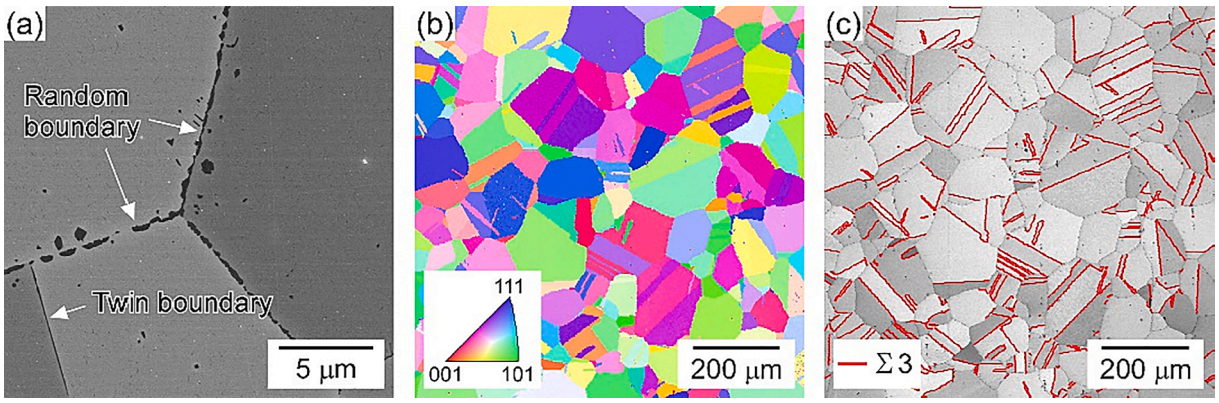

Fig. 1. (a) SEM image, (b) inverse pole figure, and (c) image quality maps of the aged steel.

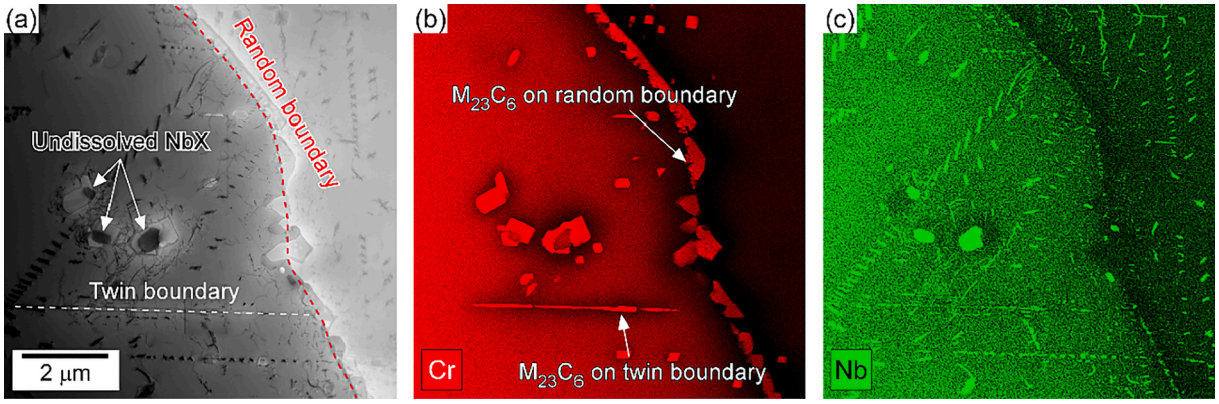

Fig. 2. (a) BF-STEM image, STEM-EDS map for (b) Cr and (c) Nb of the aged steel.

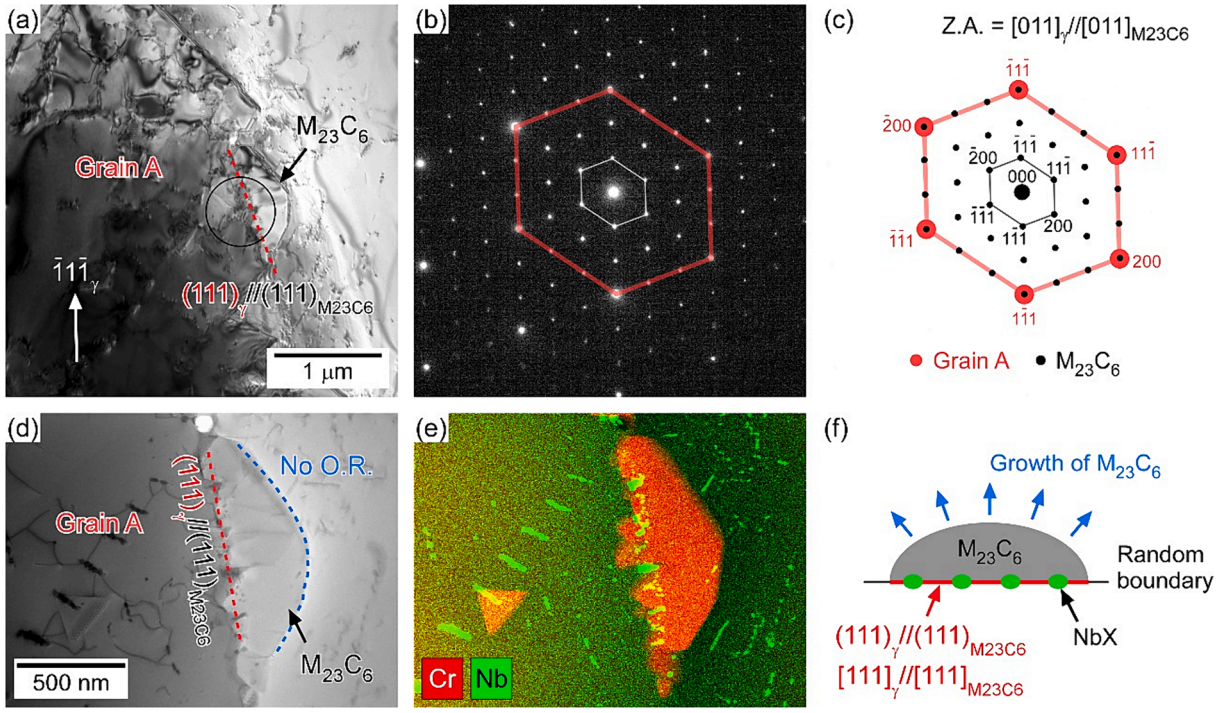

Fig. 3. (a) BF-TEM image, (b) selected area diffraction patterns (SADPs) obtained from the circular region of interest in (a), (c) indexing, (d) BF-STEM image, (e) overlaid STEM-EDS maps of Cr and Nb, and (f) schematic of the precipitation behavior on RB.

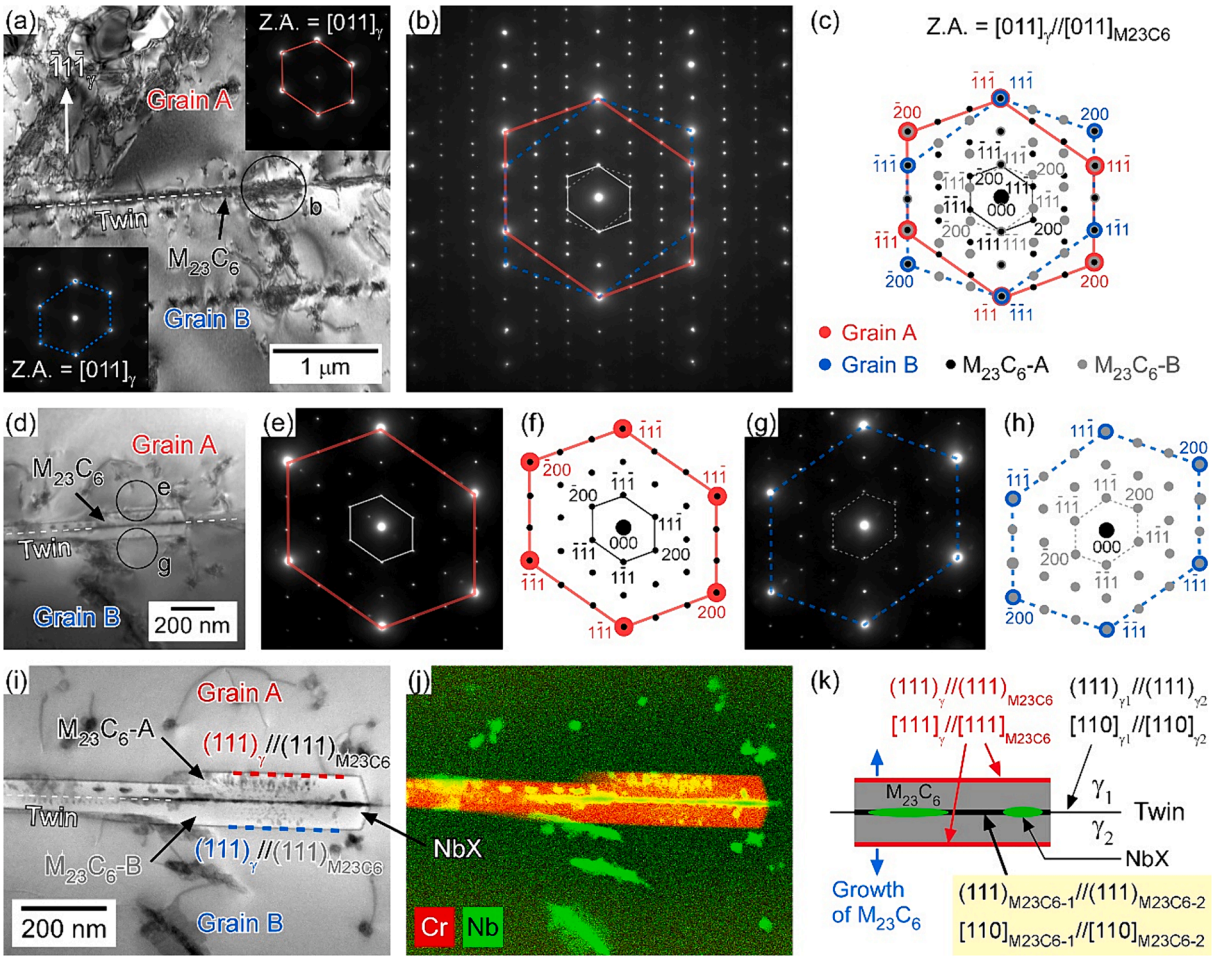

Fig. 4. (a) BF-TEM image, (b) SADP obtained from the "b" in (a), (c) indexing, (d) BF-TEM image, (e) and (g) SADPs obtained from the "e" and "g" in (d), (f) and (h) indexing, (i) BF-STEM image, (j) overlaid STEM-EDS maps of Cr and Nb, and (k) schematic of the precipitation behavior on CTB.

3. Results and discussion

Fig. 1(a) is a SEM image of the aged steel. Precipitates are observed at grain interior, RB, and CTB. Fig. 1(b) and (c) respectively show the inverse pole figure and image quality maps obtained by SEM-EBSD. Σ3 boundaries are highlighted by the red line in Fig. 1(c). The average grain diameter was approximately 130 μm when the grain tolerance angle was 5° and twin boundary was ignored. The frequency of Σ3 boundary (=length of Σ3 boundary/length of the boundary with tolerance angle > 5°) was 43 %.

Fig. 2 shows the (a) bright field (BF)-STEM image and STEM-EDS maps for (b) Cr and (c) Nb. $M_{23}C_6$ and NbX (X is mainly C and N) are precipitated in grain interior, RB, and CTB by aging. $M_{23}C_6$ was nucleated on the coarse undissolved NbX particles. The size of the $M_{23}C_6$ particles and Cr-depleted zone on RB are much larger than those on CTB, suggesting that precipitation of $M_{23}C_6$ on CTB is preferred to suppress the coarsening and sensitization by considering the inevitable precipitation of $M_{23}C_6$ during long-term creep exposure. Complete grain boundary "wetting" by $M_{23}C_6$ on CTB indicates the thermodynamic stability of the matrix/$M_{23}C_6$ interface on the CTB [11].

Fig. 3(a) is a BF-TEM image acquired around the RB. Fig. 3(b) and 3 (c) are selected area diffraction patterns (SADPs) obtained from the circular region of interest in Fig. 3(a), involving both grain-A and $M_{23}C_6$ and its indexing. $M_{23}C_6$ was coherently precipitated along (1 1 1) of grain-A with a cube-on-cube OR, even though the matrix/$M_{23}C_6$ interface was slightly serrated. Conversely, no OR was confirmed on the other side. Fig. 3(d) and (e) show the BF-STEM image and Cr + Nb map, respectively. NbX was observed at the coherent matrix/$M_{23}C_6$ interface side, and $M_{23}C_6$ was overhanging to the other side. These suggest that $M_{23}C_6$ preferentially grew toward the incoherent side of the grain, as shown in Fig. 3(f) [12,13], resulting in faster growth kinetics at RB.

Fig. 4(a) is a BF-TEM image obtained around the CTB. The insets in the upper-right and lower-left are SADPs obtained from grains-A and B, respectively. Fig. 4(b) and (c) are SADP obtained from the circular region of interest "b", involving grains-A, B, and $M_{23}C_6$ on CTB, and its indexing, respectively. The diffraction from four grains, i.e., two austenite grains (grains-A and B) and two $M_{23}C_6$ grains ($M_{23}C_6$-A and B), were obtained. Not only grain-A vs. grain-B but also $M_{23}C_6$-A vs. $M_{23}C_6$-B satisfy the OR of CTB, i.e., $(1\,1\,1)_A//(1\,1\,1)_B$ and $[1\,1\,0]_A//[1\,1\,0]_B$. In addition, both grain-A vs. $M_{23}C_6$-A and grain-B vs. $M_{23}C_6$-B satisfy the cube-on-cube OR.

Fig. 4(d) is a BF-TEM image obtained around the CTB [indicated as "b" in Fig. 4(a)]. $M_{23}C_6$ precipitated on CTB (indicated by the dashed line) extend toward the sides of both grains-A and B. SADPs obtained from the circular areas "e" and "g" in Fig. 4(d) and their indexing outcomes are shown in Fig. 4(e)–(h). They revealed that the grain-A/$M_{23}C_6$-A and grain-B/$M_{23}C_6$-B interfaces are parallel to $(1\,1\,1)_\gamma$ and $(1\,1\,1)_{M23C6}$ and satisfy the cube-on-cube OR. In other words, they have high-crack propagation arrestability [7] and slower coarsening kinetics than those of the incoherent interface. This also indicates the formation of the "$M_{23}C_6$ twin" along the original CTB of the matrix.

Fig. 4(i) and (j) are the BF-STEM image and Cr + Nb map, respectively. Faceted interfaces parallel to $(1\,1\,1)_\gamma$ and $(1\,1\,1)_{M23C6}$ are recognized on both grains-A and B. NbX is densely embedded at the $M_{23}C_6$-A/

$M_{23}C_6$-B interface. This suggests that NbX is nucleated at the original CTB of the matrix (currently $M_{23}C_6$ CTB). Nevertheless, the OR between $M_{23}C_6$ and NbX is unclear.

The precipitation behavior of $M_{23}C_6$ and NbX on CTB is schematically summarized in Fig. 4(k). Both the matrix/$M_{23}C_6$ interfaces satisfy the cube-on-cube OR with a faceted interface parallel to $(1\,1\,1)_\gamma$ and $(1\,1\,1)_{M23C6}$. The formation of $M_{23}C_6$ twin with $(1\,1\,1)_A//(1\,1\,1)_B$ and $[1\,1\,0]_A//[1\,1\,0]_B$ OR as in the austenite matrix was discovered. NbX are densely precipitated at the CTB of $M_{23}C_6$. Because all the interfaces of $M_{23}C_6$ on the CTB have good coherency, an increase in the frequency of Σ3 boundary is expected to fragment the crack propagation path and enhance the long-term creep properties.

4. Conclusions

The precipitation behaviors of $M_{23}C_6$ and NbX on RB and CTB of 25Cr-20Ni-Nb-N steel were characterized. $M_{23}C_6$ on RB satisfied a cube-on-cube OR with coherent $(1\,1\,1)_\gamma//(1\,1\,1)_{M23C6}$ interface on a single side of the matrix. NbX were nucleated at the coherent matrix/$M_{23}C_6$ interface and $M_{23}C_6$ grew toward the incoherent interface on the other side. $M_{23}C_6$ can nucleate and coarsen toward both grains belonging to CTB. Each $M_{23}C_6$ particles have $(1\,1\,1)_\gamma//(1\,1\,1)_{M23C6}$ faceted interface and satisfy a cube-on-cube OR with the matrix. As a result, coupled $M_{23}C_6$ particles on CTB satisfy $(1\,1\,1)_A//(1\,1\,1)_B$ and $[1\,1\,0]_A//[1\,1\,0]_B$. The coarsening of $M_{23}C_6$ at CTB is much slower than that in RB because of the growth toward the coherent matrix/$M_{23}C_6$ interface. Therefore, an increase in the Σ3 CSL boundary (CTB) by GBE is expected to enhance the creep properties by fragmenting the crack propagation path because CTB can maintain its coherency even after the $M_{23}C_6$ precipitation.

CRediT authorship contribution statement

Tomotaka Hatakeyama: Writing – original draft, Visualization, Methodology, Investigation, Funding acquisition, Formal analysis, Conceptualization. **Kota Sawada:** Writing – review & editing, Supervision.

Declaration of competing interest

The authors declare that they have no known competing financial interests or personal relationships that could have appeared to influence the work reported in this paper.

Data availability

Data will be made available on request.

Acknowledgements

The authors also thank Mr. Yasushi Taniuchi, Dr. Kaoru Sekido, and Mr. Takehiro Nojima for their support with heat treatments, and Mr. Taku Moronaga, Ms. Yuka Hara, and Ms. Akiko Nakamura for their support with microstructural observations (all at NIMS). This study was supported by JSPS KAKENHI [grant number JP22K14504] and Iketani Science and Technology Foundation [grant number 0351201-A].

References

[1] A. Iseda, et al., Energy Mater. 2 (2007) 199–206, https://doi.org/10.1179/174892408x382860.
[2] M. Igarashi, 25Cr-20Ni-Nb-N steel, in: K. Yagi, G. Merckling, T.-U. Kern, H. Irie, H. Warlimont (Eds.), Landolt–Bornstein - Group VIII: Advanced Materials and Technologies 2B, Springer-Verlag Berlin Heidelberg, Berlin, 2004: pp. 292–296. https://doi.org/10.1007/10837344_55.
[3] M. Yoshiba, Mater. Jpn 38 (1999) 203–211, https://doi.org/10.2320/materia.38.203.
[4] NIMS Creep Data Sheet, Metallographic Atlas of Long-term Crept Materials, No. M-12, 2019.
[5] T. Hatakeyama, K. Sawada, K. Sekido, T. Hara, K. Kimura, Mater. Sci. Eng. A 814 (2021) 141270, https://doi.org/10.1016/j.msea.2021.141270.
[6] T. Hatakeyama, K. Sawada, K. Sekido, T. Hara, K. Kimura, Mater. Sci. Eng. A 831 (2022) 142225, https://doi.org/10.1016/j.msea.2021.142225.
[7] T. Hatakeyama, K. Sawada, K. Sekido, K. Kimura, Mater. Sci. Eng. A 882 (2023) 145487, https://doi.org/10.1016/j.msea.2023.145487.
[8] T. Watanabe, J. Mater. Sci. 46 (2011) 4095–4115, https://doi.org/10.1007/s10853-011-5393-z.
[9] M. Michiuchi, H. Kokawa, Z.J. Wang, Y.S. Sato, K. Sakai, Acta Mater. 54 (2006) 5179–5184, https://doi.org/10.1016/j.actamat.2006.06.030.
[10] H.U. Hong, B.S. Rho, S.W. Nam, Mater. Sci. and Eng. A 318 (2001) 285–292, https://doi.org/10.1016/S0921-5093(01)01254-0.
[11] B.B. Straumal, A. Korneva, G.A. Lopez, A. Kuzmin, E. Rabkin, G. Gerstein, A. B. Straumal, A.S. Gornakova, Materials 14 (2021) 7506, https://doi.org/10.3390/ma14247506.
[12] H. Wen, B. Zhao, X. Dong, F. Sun, L. Zhang, Mater. Lett. 261 (2020) 126984, https://doi.org/10.1016/j.matlet.2019.126984.
[13] K. Kaneko, T. Fukunaga, K. Yamada, N. Nakada, M. Kikuchi, Z. Saghi, J.S. Barnard, P.A. Midgley, Scr. Mater. 65 (2011) 509–512, https://doi.org/10.1016/j.scriptamat.2011.06.010.